Received: 21 February 2024 | Revised: 17 September 2024 | Accepted: 19 November 2024

DOI: 10.1002/suco.202400238

ARTICLE

fib CEB-FIP WILEY

Determining the strength of 3D printed concrete with the modified slant shear test

Lucia Licciardello[1] | **Alejandro Giraldo Soto**[2] | **Walter Kaufmann**[2] | **Giovanni Metelli**[1]

[1]Department of Civil, Environmental, Architectural Engineering and Mathematics, University of Brescia, Brescia, Italy

[2]Institute of Structural Engineering (IBK), ETH Zurich, Zurich, Switzerland

Correspondence
Lucia Licciardello, Department of Civil, Environmental, Architectural Engineering and Mathematics, University of Brescia, via Branze 43, Brescia, Italy.
Email: l.licciardello@unibs.it

Funding information
Swiss National Science Foundation (project number 51NF40-205604); University of Brescia

Abstract

This study deals with the assessment of the load-bearing capacity of layered 3D printed concrete (3DPC) using a modified slant shear test (MSST) to define a Mohr's envelope. To this aim, the established modified Coulomb yield condition of the concrete is complemented by a Coulomb failure criterion of the layer joints (cold or dry joints). Due to the anisotropy inherent to 3DPC elements, caused by the interlayer of printed concrete, the test setups commonly used for conventional concrete are inadequate to assess the load-bearing capacity of 3DPC. A total of 45 3DPC specimens with different inclinations of the concrete printed layers, including a cold joint with 30 min time gap were tested using the MSST. The results showed a high strength of the interfaces with two different failure modes, depending on the inclination of the layers: (i) concrete matrix failure and (ii) layer interface failure, where the latter governed for layer inclinations of 60° and 75° with respect to the horizontal plane. The test campaign confirms that the proposed MSST is a highly practical test method that enables determining the parameters governing a Mohr's envelope of layered 3DPC and can thus be used to reliably characterize its load-bearing capacity.

KEYWORDS

3D concrete printing, 3DPC interlayer strength, cold joint, dry joint, load-bearing 3DPC, modified slant shear tests, Mohr's failure envelope of 3DPC

1 | INTRODUCTION

1.1 | Overview

Nowadays, 3D printed concrete (3DPC) is mainly used as non-load-bearing elements, either as lost formwork to cast complex geometries (e.g., curved walls and bespoke columns), or to conceive hybrid structures,[1,2] rather than being fully integrated as part of load-bearing structures. This is primarily due to the lack of a design basis for load-bearing 3DPC, including the uncertainty related to the effect of the layer joints on the concrete strength, and the difficulty to arrange reinforcement. These issues must be addressed in order to facilitate the use of load-bearing 3DPC, enabling highly material-efficient structures by reducing the wall thickness of structural elements to a minimum and hence, benefiting from the related reduction of CO_2 emissions (reduced material use, particularly concrete and hence, cement) and fabrication waste.[3,4]

While the integration of reinforcement in 3DPC has recently received considerable attention,[5–15] little research has targeted the fact that the bases of design for conventional concrete cannot be directly applied due to the anisotropy inherent to 3DPC elements caused by the printing process.[16,17] Specifically, while numerous 3DPC tests have been carried out using various setups to evaluate the 3DPC strength,[18–25] and several mechanical models, such as the modified Mohr-Griffith compression-shear constitutive model for 3DPC[26] or the Mohr-Coulomb failure[27] have also been considered. Neither a specific failure criterion nor a practical test method has yet been established to reliably characterize the load-bearing capacity of layered 3DPC, accounting for the anisotropy caused by the interlayer behavior.

The present paper addresses these issues by proposing a modification of the standard method for determining slant shear strength,[28] and using this modified test method to characterize the load-bearing capacity of layered 3DPC specimens in plane stress by means of a Mohr's envelope.

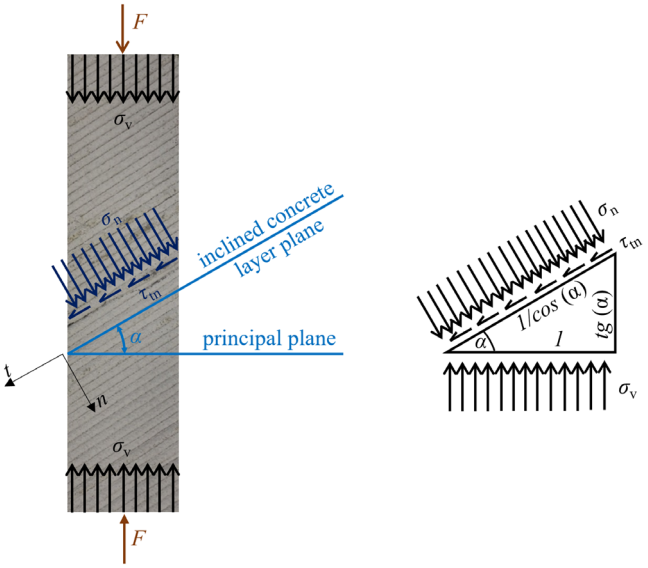

FIGURE 1 3D printed concrete specimen with definition of layer inclination α and stresses acting on the layer plane: σ_v are the applied vertical stresses; σ_n and τ_{tn} are the normal and shear stresses at the interface between concrete layers.

1.2 | Particularities of 3DPC

Mechanically, 3DPC differs from ordinary cast concrete primarily by (i) a much smaller aggregate size (which strictly speaking qualifies as fine mortar, rather than concrete) and (ii) the presence of joints between layers. As the layer joints are weaker than the concrete matrix, they cause an anisotropy that affects the load-bearing capacity and the failure mode: in addition to concrete matrix failures along a failure surface depending on the stress state, layer interface failure may occur. The strength and the failure modes of 3DPC thus not only depend on the material properties of the concrete matrix as in conventionally cast elements but also on the behavior of the layer joints. The latter is governed by the interface characteristics—which depend on the concrete matrix, the interval time between the layers, and the possible presence of voids between the layers—as well as the orientation of the layers with respect to the principal stress directions, which can be defined by the ratio of shear to normal stresses acting on the interlayer plane (see Figure 1).

Adopting a Coulomb failure criterion,[29] the strength of the interfaces can be characterized by the angle of internal friction of the matrix φ_c, the angle of friction between the concrete layers φ_i (cold and dry joints), and the cohesion c, which are also established parameters for characterizing the strength of the concrete matrix.[30] Throughout the text, the terminology angle of friction will be used for both the matrix and the concrete layers. Based on numerous studies on conventionally cast concrete, it is well-known that these parameters are directly related to the concrete compressive strength and are affected by several properties of the concrete mix (aggregate size, porosity, shrinkage, age, etc.).[30,31] However, there is a lack of research in the literature that focuses on the effect of 3D printing.

In Jayathilakage et al.,[27] the mechanical parameters of a concrete mix designed for 3D printing were assessed through direct shear tests on cast specimens, yielding angles of (internal) friction of 45°... 55°. In van den Heever et al.,[26] the shear properties of a fiber-reinforced printable concrete were assessed through direct shear tests. Small 3DPC cylinders (Ø21.6 × 20 mm) were tested by applying the shear load in different directions with respect to the concrete layers. An angle of (internal) friction of around 45° was found for both cast and layered specimens. Regarding the interlayer interval time, it has been shown experimentally that the compressive and flexural strength may be affected by the interval time of the printing process, which was varied up to 24 h.[23,32] Further research studies indicated that with an interlayer interval time between 10 and 30 min, the material properties are similar.[33] In addition, the presence of voids can have a significant impact. Such voids typically result from the printing of adjacent filaments, which may be required depending on the width of the printed layers and the specific object to be printed: the required wall thickness may exceed that of a single filament, and in some cases the choice of a several narrow instead of one wider filament,

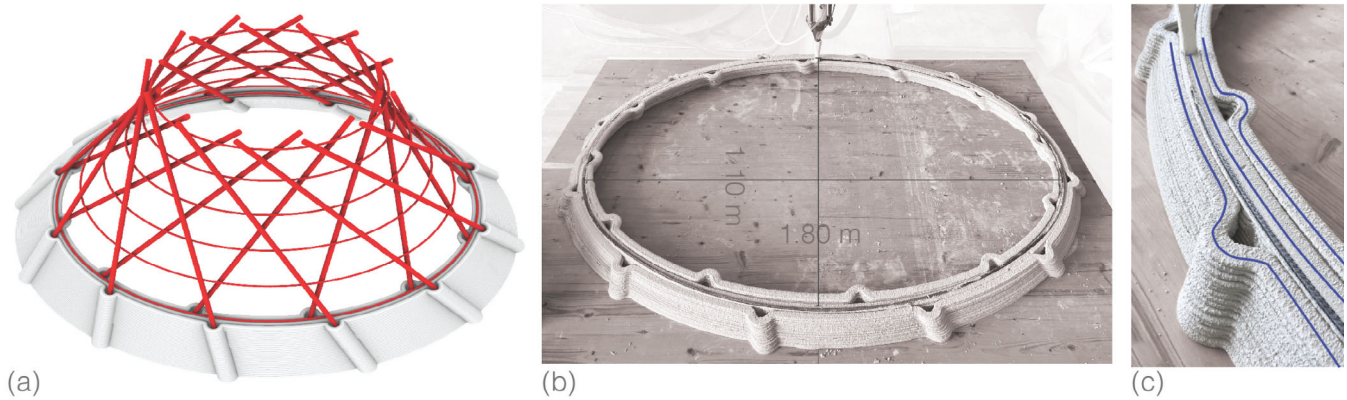

FIGURE 2 Layer joints, print-paths, and reinforcement concept for an elliptic hyperbolic column and interlayer rebar: (a) vertical and horizontal reinforcing bar layout; (b) placement of one interlayer reinforcing bar ring during 3D printed concrete; (c) print path with three adjacent parallel filaments per layer.[35]

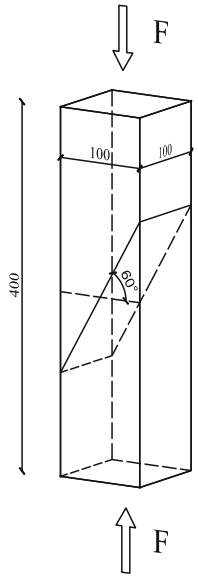

FIGURE 3 Slant shear test to evaluate the strength of the interface between concrete layers cast at different times.[28]

hence using a smaller extruder radius, facilitates the optimization of complex geometries (e.g., bespoke columns[1,34,35]) and enables the printing of holes for reinforcement purposes (see Figure 2).

1.3 | Modified slant shear test

In conventional concrete, the slant shear test (Figure 3) is used to study the interfacial bond strength between concrete cast at different times, or concrete and a repair material[36] (e.g., adhesives) by conducting uniaxial compression tests on prisms with an interface plane oriented at an angle of $\alpha = 60^\circ$ to the horizontal.[28] It was initially introduced by the University of Arizona,[37] using a composite cylinder, and successively, Tabor[38] used prismatic specimens for the test. Currently, specimens of different sizes and geometries are employed, and the bond strength between the substrate and the repair material was investigated by considering different inclinations of the bond plane. Different shear-normal stress ratios at the interface were investigated by loading the specimen in compression.[39–41] It has been shown that the shear strength as well as the failure mode, which may occur by either layer interface or matrix failure, is influenced by various factors such as the interface angle,[39–41] interface roughness,[42] differential stiffness between the layers,[43] specimen dimension, and curing conditions,[40] among others.

While the slant shear test is widely used, other test methods, such as the bi-surface test and the push-out test, are also used to assess the bond strength. Several studies have compared the results obtained from these different tests. According to the research of Momayez et al.[42] and Zanotti and Randl,[39] the strength measured with the slant shear test resulted higher than that obtained with the bi-surface shear test[42] or the push-out test.[39] This increase in strength might be attributed to increased interlock and friction at the interface caused by the compressive stresses generated during the test.

Some recent research studies proposed variations of the slant shear test. The study by Saldanha et al.[44] proposed a version of the slant shear test that ensures a layer interface failure by reinforcing the upper and lower parts of the specimens. Monolithic (no joints) specimens, both unreinforced and reinforced, were tested, showing matrix and layer interface failure, respectively. Hua et al.[45] investigated the effect of shear key angles and shear joint inclinations of 3DPC shear keys. The specimens were tested at different interface inclinations and exhibited a failure mode that involved layer interface and matrix failure. The results of these tests were also compared with

push-off tests, which gave unexpectedly higher results. In fact, during the slant shear test, some specimens experienced a non-uniform compressive load transfer due to dimensional variations in the 3DPC filaments, leading to slight bending and reduced peak shear strength compared to that obtained from push-off test.

This established test method is adapted in this study to the modified slant shear test (MSST), as illustrated in Figure 3, by varying the layer plane inclination α.

The anisotropy of 3DPC caused by the printing process can be captured by carrying out a series of MSST with varying layer plane inclinations α, determining the shear transfer capacity across the layer joints for different stress states. Based on the results of a MSST series with varying layer plane inclination α, the interface behavior and, hence, the direction-dependent load-bearing capacity of 3DPC, the corresponding strength parameters and the failure modes can readily be obtained.

2 | EXPERIMENTAL CAMPAIGN

An experimental campaign was conducted at ETH Zurich (2022) to investigate the load-bearing capacity of 3DPC. The MSST was used to determine the 3DPC strength, accounting for the influence of the anisotropy generated by the printed concrete layers. A total of 45 3DPC specimens were tested at various ages (7, 14, and 28 days after printing). As specified in EN 12615:1999,[28] the specimens consisted of 3DPC prisms 400 mm high with a square 100×100 mm^2 cross-section. A variety of concrete layer inclinations α to the horizontal plane (instead of only one constant inclination of 60° according to the standard[28]) were considered. It should be noticed that each specimen included a cold joint with 30 min time gap.

Note that the proposed MSST aims to evaluate the 3DPC performance, taking into account the influence of the concrete layer interface, which can be of different types, dry or cold, with different time gaps, with treatments or including adhesives, among others. The MSST also allows the study of other parameters, such as roughness and curing conditions, among others, that may influence the strength of the concrete layer interface. However, this study does not examine these parameters and focuses on presenting the results obtained from the specimens produced as described in the following sections.

2.1 | Material

The 3D printing mortar used for the specimens consists of a dry mix that includes white Portland cement (CEM I 42.5R) at a proportion of 525 kg/m^3 combined with limestone (<125 μm) and three grades of quartz sand (<0.1, 0.1–0.6, and 0.6–1.25 mm). A superplasticizer and a viscosity modifier are also added in dry form, dosed to the cement content. The water-to-cement ratio is 0.5. The accelerator is a slurry of white calcium aluminate cement and calcium sulfate anhydrite (1:2.1 ratio) at a water-to-powder ratio of 0.35. The thickener is based on a sodium metasilicate solution and a starch ether-based viscosity modifier. The accelerator and thickener are dosed at the printhead at standard ratios of 0.05 and 0.01 by mass of the concrete flow rate, respectively. The three components can be adjusted throughout the process depending on room conditions, with the accelerator dominating strength buildup behavior and the thickener dominating initial yield stress, which governs the filament shape.[46] Be aware that the maximum aggregate size of the material used within this study is below 4 mm; therefore, the cement-based material used in this research may be defined as "high-strength mortar." However, the term "concrete" is preferred throughout this manuscript, as commonly used in the literature on 3DPC.

The flexural tensile and compressive strengths of the 3DPC were determined at 7, 14, and 28 days by testing three cast concrete specimens ($160 \times 40 \times 40$ mm^3) at each concrete age, according to EN 1015-11:2020.[47] The specimens were printed and cured in laboratory environment with a temperature of 20° and a humidity of 45%. The flexural tensile strength $f_{ctm,fl}$ was determined by three-point bending tests (Figure 4a,b), and the compressive strength f_{cm} was obtained from uniaxial compression tests on the broken pieces of the three-point bending tests (Figure 4c).

The compressive strength of the concrete f_{cm} is determined by:

$$f_{cm} = \frac{F_{max}}{b\, l_p}, \tag{1}$$

where l_p is the width of the loading plate (40 mm).

The flexural tensile strength of the concrete $f_{ctm,fl}$ is determined by:

$$f_{ctm,fl} = \frac{3}{2}\frac{F_{max}\, l}{b\, h^2}, \tag{2}$$

where F_{max} is the maximum load of the three-point bending test, $\underline{l}$ is the distance between the supports (100 mm ± 0.5 mm), and $\underline{h}$ and $\underline{b}$ are the depth (40 mm) and the width (40 mm) of the concrete specimen, respectively. The tensile strength f_{ctm} of 3DPC is estimated based on the flexural tensile strength according to Eurocode 2[48] as:

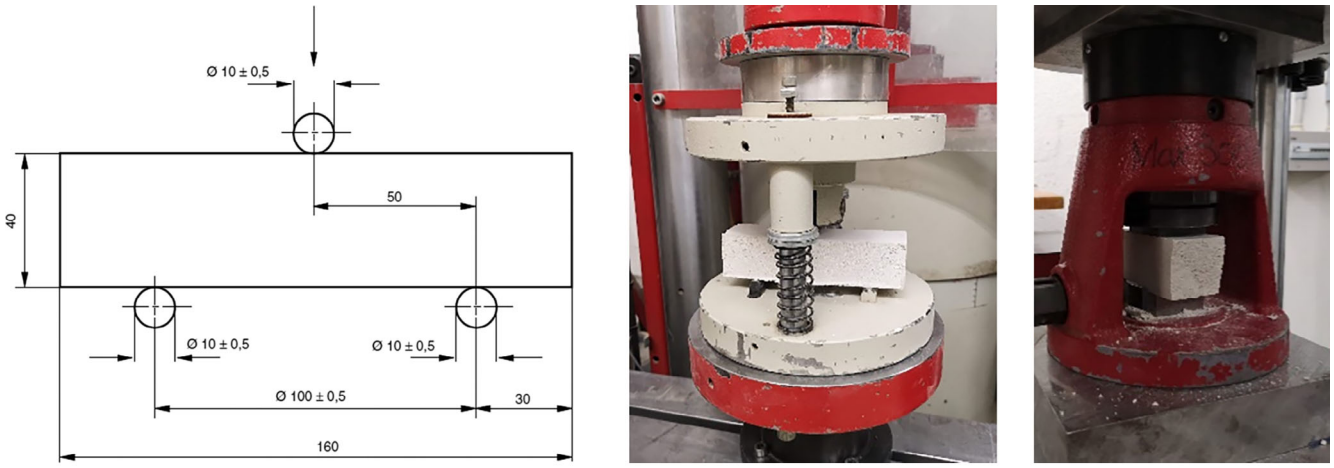

FIGURE 4 Concrete beam test: (a) specimen; (b) three-point bending test; and (c) compression test.

TABLE 1 Flexural tensile strength $f_{ctm,fl}$, compressive strength f_{cm}, and estimated tensile strength f_{ctm} of the 3D printed concrete.

Concrete age	$f_{ctm,fl}$[a] (MPa)	f_{cm}[a] (MPa)	f_{ctm}[b] (MPa)	f_{cm}/f_{ctm} (-)
7 days	9.6	57.7	6.15	9.4
14 days	10.7	63.7	6.86	9.3
28 days	12.7	66.2	8.14	8.1

[a]According to EN 1015-11:2020.[47]
[b]According to Eurocode 2.[48]

$$f_{ctm,fl} = \max\left\{\left(1.6 - \frac{h}{1000}\right) f_{ctm}; f_{ctm}\right\},$$
$$f_{ctm} = \min\left\{\frac{f_{ctm,fl}}{(1.6 - (h/1000))}; f_{ctm,fl}\right\}, \quad (3)$$

where h is the total member depth and f_{ctm} is the mean tensile strength. Table 1 compiles the flexural tensile strength $f_{ctm,fl}$, the compressive strength f_{cm}, and the estimated tensile strength f_{ctm} of the specimens tested at 7, 14, and 28 days according to EN 1015-11:2020.[47] The averages of the estimated tensile strength f_{ctm} are 6.15, 6.86, and 8.14 MPa at 7, 14, and 28 days, respectively, with an average ratio f_{cm}/f_{ctm} of about 9, which is in the same range as expected for conventional cast concrete ($f_{cm}/f_{ctm} \simeq 10$ for uniaxial compression test). It should be noted that tensile strength back-calculated from the flexural tensile strength and the double-punch tests are significantly higher and lower, respectively, as observed in Soto et al.[49]

2.2 | Specimens

The specimens were produced at ETH Zurich using a robotic arm equipped with a printing nozzle and cured in a laboratory environment with a temperature of 20° and a humidity of 45%. Detailed information on the printing setup can be found in Refs. 1,34. To be able to produce the 3DPC specimens for MSST with the dimensions 100 × 100 × 400 mm^3 as specified for the standard slant shear test by Ref. 28, but with several concrete layer inclinations (Figure 2), they were cut out of 3DPC walls of 100 mm thickness and variable height and length (Figure 5a). A single printed concrete layer was formed by a 25 mm wide filament and 7 mm thick print-path, that is, the 100 mm wall width consisted of four adjacent parallel filaments (Figure 5a,b) printed using a suitable print path. To consider a certain tolerance of possible interruption during the production of 3DPC elements, a cold joint with 30 min time gap, referred to in the following as *Cold Joint-30*, was introduced at approximately half height of the 3DPC specimens (indicated as a dotted black line in Figure 5c) by pausing the printing. The surface of *Cold Joint-30* was essentially smooth, as it was not subjected to any treatment.

The specimens, cut from the 3DPC walls (Figure 5c), consisted of 3DPC prisms 400 mm high with a 100 × 100 mm^2 square cross-section, with different concrete layer inclinations $\alpha = 0°$, 30°, 60°, 75° and 90° (Figure 6) and *Cold Joint-30* at half height. The real dimensions of the specimens varied from 398 to 405 mm coefficient of variation (CoV 0.93%), from 96 to 106 mm (CoV 4.9%) and from 106 to 119 mm (CoV 5.5%) considering the height, the length, and the width, respectively.

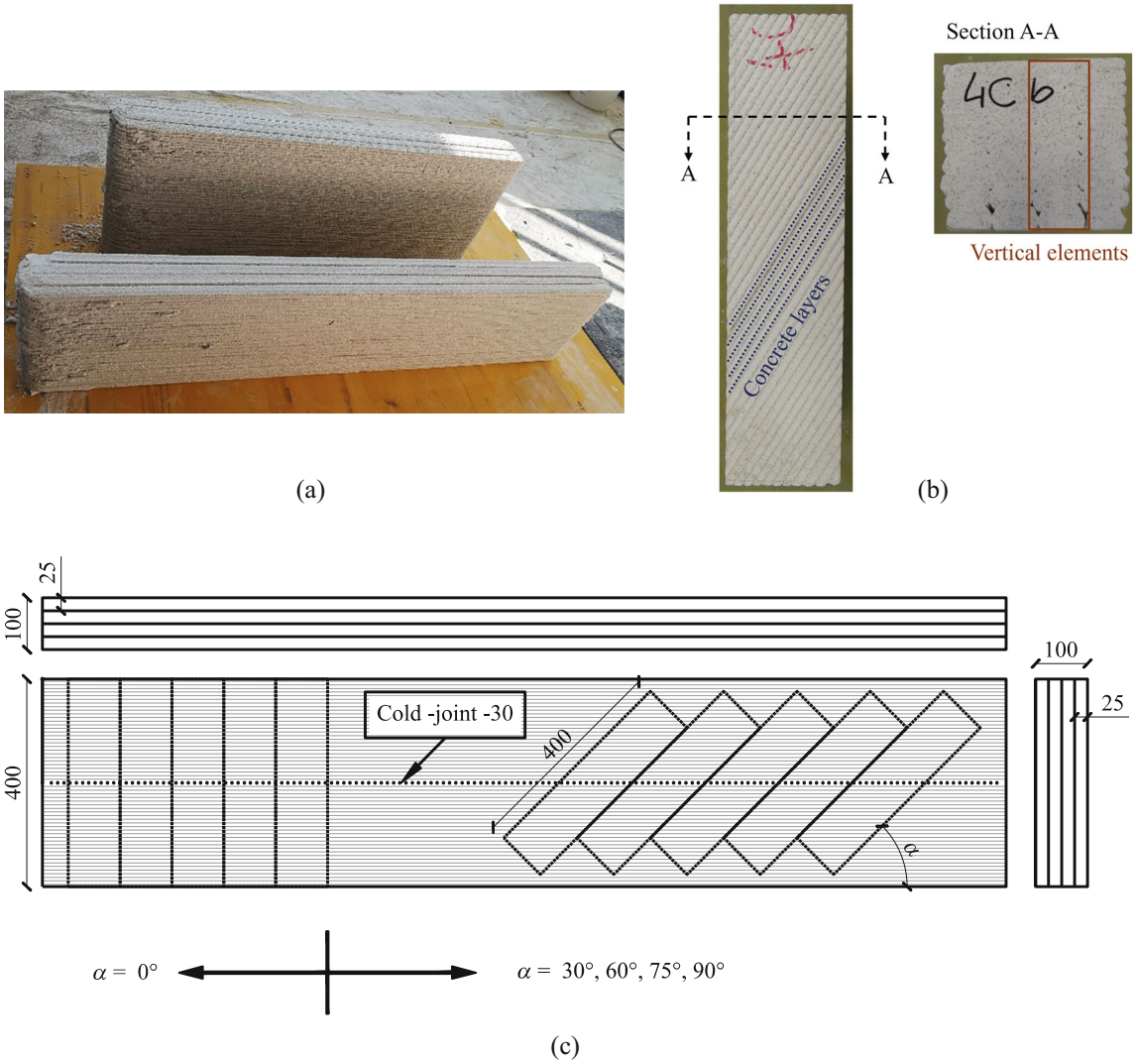

FIGURE 5 (a) 3D printed concrete walls with Cold Joint-30; (b) specimen cross-section; and (c) example of the cutting layout of the specimens.

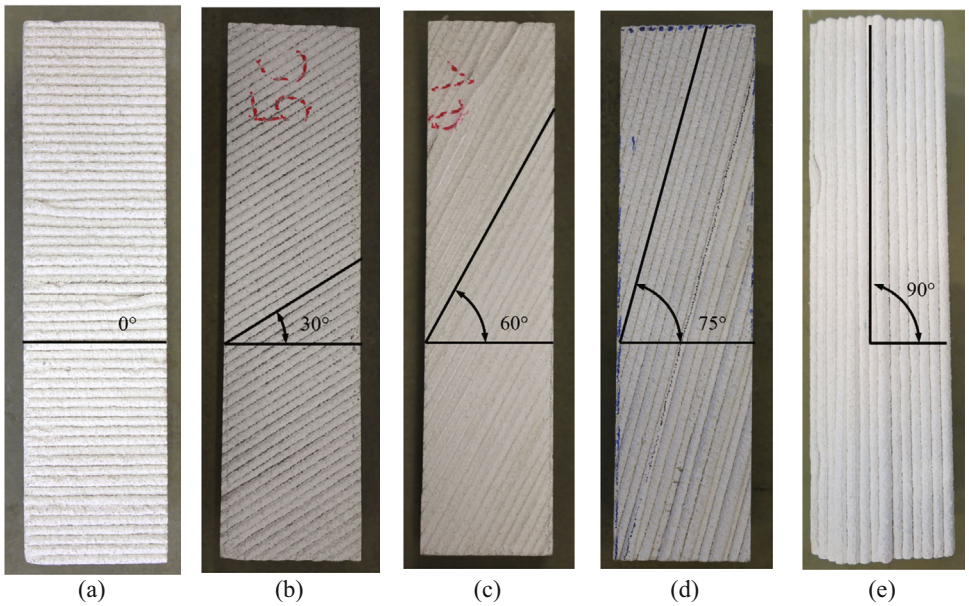

FIGURE 6 3D printed concrete specimens with different concrete layer inclinations to the horizontal plane: (a) 0°; (b) 30°; (c) 60°; (d) 75°; and (e) 90°.

TABLE 2 Overview of the experimental campaign. Specimen designation: production (P = 3D printed concrete [3DPC])-inclination-time gap (in hours)-surface finishing (N = normal, no interface treatment)-concrete age (days).

Designation	Number of tests (–)	Production (–)	Inclination α (°)	Time gap (h)	Surface finishing (–)	Concrete age (days)
P-00-0.5-N-07	3	3DPC	0	0.5	Normal	7
P-00-0.5-N-14	3	3DPC	0	0.5	Normal	14
P-00-0.5-N-28	3	3DPC	0	0.5	Normal	28
P-30-0.5-N-07	3	3DPC	30	0.5	Normal	7
P-30-0.5-N-14	3	3DPC	30	0.5	Normal	14
P-30-0.5-N-28	3	3DPC	30	0.5	Normal	28
P-60-0.5-N-07	3	3DPC	60	0.5	Normal	7
P-60-0.5-N-14	3	3DPC	60	0.5	Normal	14
P-60-0.5-N-28	3	3DPC	60	0.5	Normal	28
P-75-0.5-N-07	3	3DPC	75	0.5	Normal	7
P-75-0.5-N-14	3	3DPC	75	0.5	Normal	14
P-75-0.5-N-28	3	3DPC	75	0.5	Normal	28
P-90-0.5-N-07	3	3DPC	90	0.5	Normal	7
P-90-0.5-N-14	3	3DPC	90	0.5	Normal	14
P-90-0.5-N-28	3	3DPC	90	0.5	Normal	28

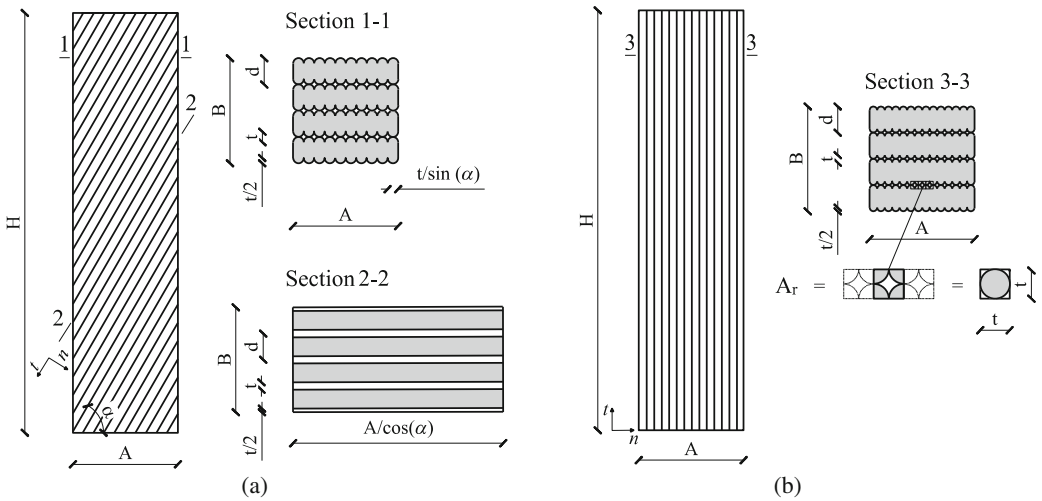

FIGURE 7 Sections in horizontal and inclined planes and geometric parameters to calculate the effective areas ($A_{h,eff}$ and $A_{n,eff}$) of the specimens. (a) $\alpha = 0°$, 30°, 60°, and 75°; (b) $\alpha = 90°$.

The nominal dimensions of the specimens are used to determine the cross-sectional areas in the following. For each interlayer inclination ($\alpha = 0°$, 30°, 60°, 75°, and 90°), three groups of three specimens each were tested at 7, 14, and 28 days after the printing, resulting in a total of 45 prisms. Table 2 summarizes the experimental campaign, including the specimen designation, indicating the type of production (P for 3DPC), the concrete layer inclination (α), the time gap in hours of the cold joint (0.5), the finishing of the surface (N for normal = no treatment), and the concrete age at testing. Note that in the present study, only layer inclination and concrete age were varied, but future test campaigns addressing the effect of further parameters are planned.

Figure 7 shows the horizontal and inclined sections (parallel to printed layers) of the tested specimens with concrete layer inclinations $\alpha = 0°$ ... 75° (Figure 7a) and vertical concrete layer inclinations ($\alpha = 90°$; see Figure 7b). Due to the fabrication process, the two external faces of the 3DPC specimens that had not been cut exhibited wavy surfaces caused by the printed concrete layers (Figure 7). Furthermore, it should be noted that the 3DPC specimens were not fully solid but internal voids were located between the filaments (print-paths), that is, three vertical wavy interfaces formed

by the contact of two wavy surfaces (Figure 7a,b) each. This was a consequence of the choice to use a small extruder radius as commonly required for the printing of complex geometries.[34,35] Consequently, a reduced or effective cross-sectional area of each specimen is taken into account to estimate the 3DPC strength, accounting for the fact that the internal voids and all surface waves do not contribute to the strength (white shaded areas in section 1-1 of Figure 7). While the wave radius is variable due to printing imperfections, an average wave radius equal to the targeted 7 mm concrete layer thickness was considered for simplicity. Two effective cross-sectional areas are distinguished: (i) the effective horizontal area $A_{H,eff}$, that is, corresponding to the cross-section perpendicular to applied vertical force F (sections 1-1 and 3-3), and (ii) the effective slanting area $A_{n,eff}$, which corresponds to the cross-sections contained in the inclined interface planes n (section 2-2), see Figure 7a.

The effective horizontal area $A_{H,eff}$ and the effective slanting area $A_{n,eff}$ for the specimens with concrete layer inclinations $\alpha = 0° \ldots 75°$ are given by:

$$A_{H,eff} = A \cdot B \cdot \left(1 - \frac{t}{d}\right),$$
$$A_{n,eff} = A \cdot B \cdot \left(\frac{1}{\cos\alpha} - \frac{t}{d}\right), \quad (4)$$

respectively, where A and B are the nominal dimensions of the cross-section (equal to 100 mm), t is the thickness (7 mm), and d the width (25 mm) of the filament, and α is the concrete layer inclination to the horizontal plane in the slant shear test specimen.

The effective horizontal area $A_{H,90,eff}$ (section 3-3) for the specimens with a vertical concrete layer inclination ($\alpha = 90°$) is calculated by:

$$A_{r,tot} = \frac{A}{t} \cdot \frac{B}{d} \cdot \left(t^2 - \frac{\pi t^2}{4}\right) = A \cdot B \cdot \frac{t}{d}\left(1 - \frac{\pi}{4}\right)$$
$$A_{H,90,eff} = A \cdot B - A_{r,tot} = A \cdot B \cdot \left[1 - \frac{t}{d}\left(1 - \frac{\pi}{4}\right)\right], \quad (5)$$

where $A_{r,tot}$ is the total area of the voids between the four parallel vertical layers created by the print-paths (Figure 5b).

2.3 | Test setup

Figure 8 shows the test setup of the MSST for 3DPC, which essentially is a uniaxial compression test on 3DPC prisms ($400 \times 100 \times 100\ mm^3$) with different concrete layer inclinations. The 3DPC tests were carried out using a servo-hydraulic universal testing machine with a capacity of 1600 kN. The 3DPC specimens were placed in a vertical position (Figure 8) and subjected to axial compression in displacement control with a rate of 0.2 mm/min.

3 | RESULTS

Figure 1 shows the stresses on a horizontal and on an inclined section of the 3DPC specimens subjected to a vertical compressive force F: σ_v are the vertical stresses (normal stresses on a horizontal plane), while σ_n and τ_{tn} are the normal and shear stresses acting on the interface section between 3DPC layers, inclined at an angle α to the horizontal, respectively. These stresses are calculated as follows:

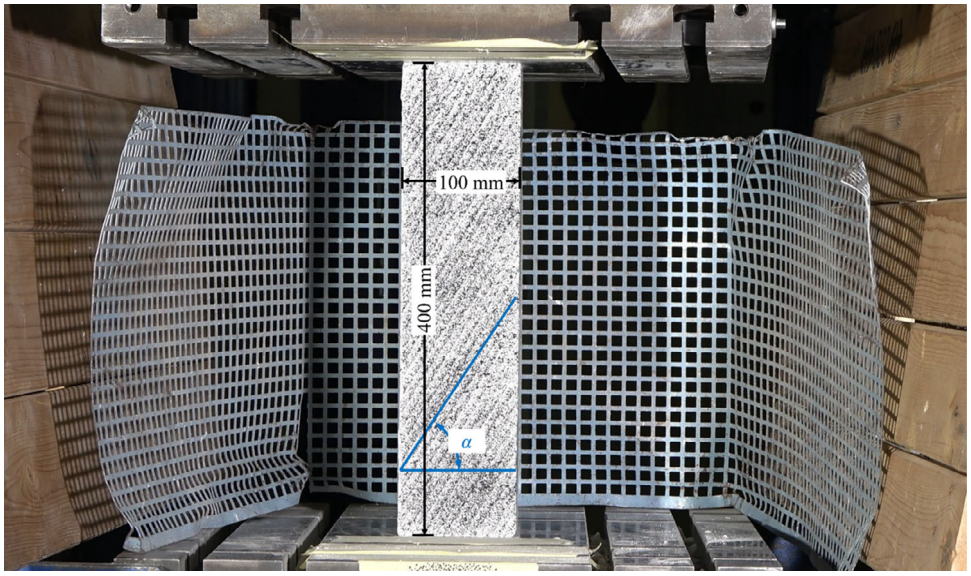

FIGURE 8 Test setup of the modified slant shear test for 3D printed concrete.

$$\sigma_v = \frac{F}{A_{H,eff}} (\alpha = 0° ... 75°)$$
$$\sigma_v = \frac{F}{A_{H,90,eff}} (\alpha = 90°), \quad (6)$$

$$\sigma_n = \sigma_v \cos^2 \alpha, \quad (7)$$

$$\tau_{tn} = \sigma_v \sin \alpha \cos \alpha, \quad (8)$$

where $A_{H,eff}$ and $A_{H,90,eff}$ are the effective horizontal areas calculated according to Equations (4) or (5) depending on the concrete layer inclinations.

Table 3 and Figure 9 show the mean stresses (the standard deviation is reported in parentheses) in the horizontal and inclined planes ($\sigma_{v,m}$, $\sigma_{n,m}$, and $\tau_{tn,m}$) for the peak compression force F_{max} obtained from the three tested specimens of each series for a given concrete layer inclination and concrete age (excluding those with no representative results, for example, due to excessive imperfections). Depending on the layer inclination, two different failure modes were observed (see Table 3): (i) matrix failure (Figure 10a,b,e), and (ii) layer interface failure. While the specimens with layer inclinations of 0°, 30°, and 90° exhibited matrix failures, layer interface failures occurred at the *Cold Joint-30* of the specimens with

TABLE 3 Modified slant shear test results: maximum force F_{max}, mean vertical stresses $\sigma_{v,m}$, mean normal $\sigma_{n,m}$, and mean shear stresses $\tau_{tn,m}$ in the interfaces between concrete layers. Shading highlights specimens with layer interface failure. Standard deviation "()."

α (°)	Designation (-)	Days (-)	Failure	F_{max} (kN)	$\sigma_{v,m}$ (MPa)	$\sigma_{n,m}$ (MPa)	$\tau_{tn,m}$ (MPa)
0	P-00-0.5-N-07	7 days	Matrix	462.86 (5.70)	−57.66 (2.51)	−57.66 (2.51)	-
	P-00-0.5-N-14	14 days	Matrix	543.24 (14.89)	−68.49 (1.75)	−68.49 (1.75)	-
	P-00-0.5-N-28	28 days	Matrix	412.64 (25.94)	−53.47 (2.90)	−53.47 (2.90)	-
30	P-30-0.5-N-07	7 days	Matrix	528.03 (13.56)	−65.66 (0.81)	−49.24 (0.61)	28.43 (0.35)
	P-30-0.5-N-14	14 days	Matrix	681.22 (10.97)	−85.78 (1.25)	−64.34 (0.94)	37.14 (0.54)
	P-30-0.5-N-28	28 days	Matrix	621.97 (35.69)	−78.99 (3.19)	−59.24 (2.39)	34.20 (1.38)
60	P-60-0.5-N-07	7 days	Layer interface	469.76 (71.56)	−58.52 (9.02)	−14.63 (2.25)	25.34 (3.90)
	P-60-0.5-N-14[a]	14 days	Layer interface	633.33 (−)	−77.86 (−)	−19.46 (−)	33.71 (−)
	P-60-0.5-N-28	28 days	Layer interface	510.15 (85.38)	−64.16 (11.11)	−16.04 (2.78)	27.78 (4.81)
75	P-75-0.5-N-07	7 days	Layer interface	443.88 (18.38)	−56.25 (1.57)	−3.77 (0.11)	14.06 (0.39)
	P-75-0.5-N-14	14 days	Layer interface	584.63 (4.35)	−73.52 (2.74)	−4.92 (0.18)	18.38 (0.69)
	P-75-0.5-N-28	28 days	Layer interface	496.89 (95.84)	−62.27 (11.76)	−4.17 (0.79)	15.57 (2.94)
90	P-90-0.5-N-07	7 days	Matrix	640.33 (14.29)	−55.00 (1.44)	-	-
	P-90-0.5-N-14	14 days	Matrix	647.12 (50.72)	−59.36 (4.52)	-	-
	P-90-0.5-N-28	28 days	Matrix	665.40 (14.13)	−59.29 (2.69)	-	-

[a]Only one specimen with acceptable result (see Appendix A).

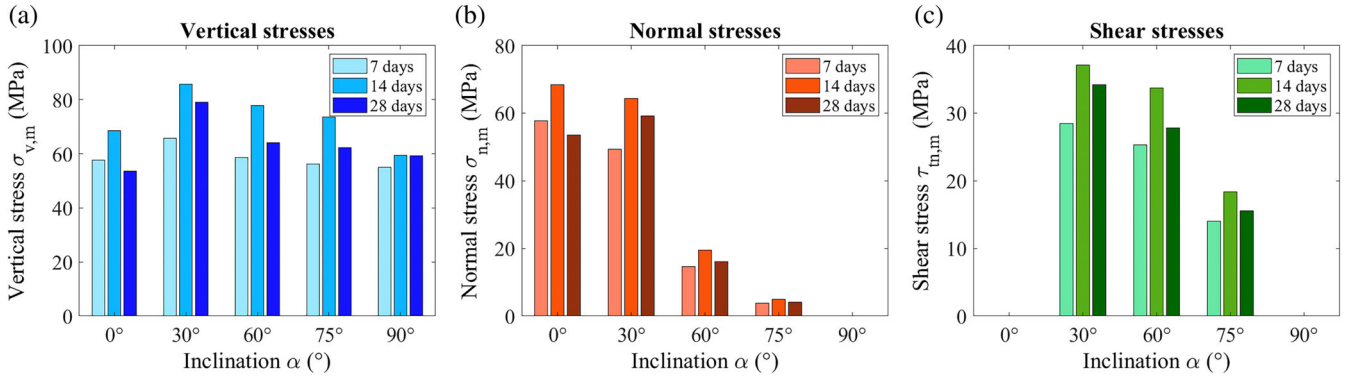

FIGURE 9 Mean stresses for different concrete layer inclinations: (a) mean vertical stress $\sigma_{v,m}$; (b) mean normal stresses $\sigma_{n,m}$ in the inclined planes; (c) mean shear stresses $\tau_{tn,m}$ in the inclined planes.

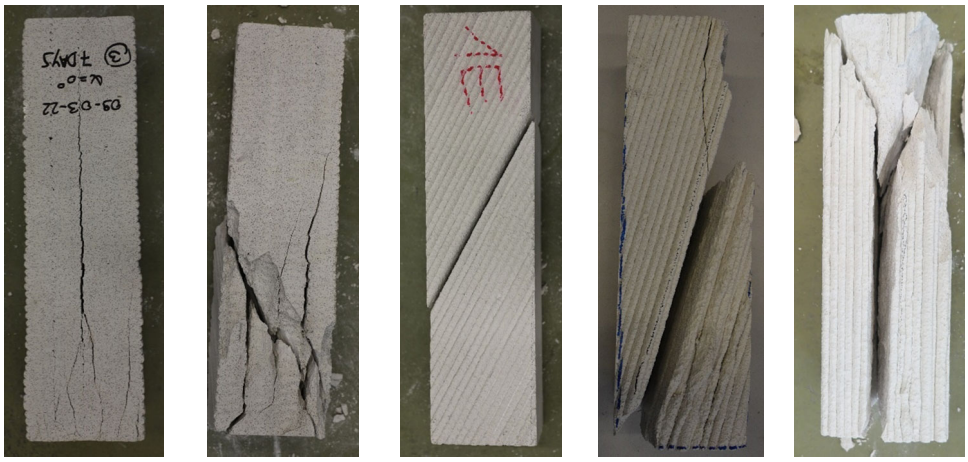

(a) $\alpha = 0°$ (b) $\alpha = 30°$ (c) $\alpha = 60°$ (d) $\alpha = 75°$ (e) $\alpha = 90°$

FIGURE 10 Typical failure modes for different layer inclinations.

concrete layer inclinations of 60° (Figure 10c) and 75° (Figure 10d), see also Table 3.

The maximum mean normal stress $\sigma_{v,m}$ (Figure 9a) ranged from −55 to −65, −60 to −85, and −53 to −78 MPa at 7, 14, and 28 days after the printing, respectively, indicating that the 3DPC had gained its full strength 14 days after the printing. While about 80% of the maximum strength was already reached at 7 days, the experimentally observed 3DPC strength at an age of 28 days was slightly lower than at 14 days. Apart from experimental scatter, this unexpected result can be attributed to the imperfections and irregularities in the cuts and printing patterns, which were generally more pronounced in the specimens tested at 28 days than in those tested at other concrete ages. Furthermore, for the specimens with horizontal concrete layers ($\alpha = 0°$), the printing imperfections in the faces of force application (the load application faces lacked smoothness and uniformity since they were not cut) also affected the bearing capacity since the four parallel filaments (Figure 5b) were not uniformly loaded, causing certain stress concentrations. Therefore, a significantly lower strength (reduction of about 10%, 20%, and 30% at 7, 14, and 28 days, respectively) was observed compared to the specimens with $\alpha = 30°$ (Figure 10b), which also failed by crushing of the concrete matrix. The specimens with vertical concrete layers ($\alpha = 90°$) also exhibited an appreciably lower strength (reduction of about 15%, 30%, and 25% at 7, 14, and 28 days, respectively) than those with $\alpha = 30°$. In this case, the concrete matrix failure was accompanied by a debonding in the vertical layer interfaces, similar to failures by laminar splitting common in compression tests on high-strength concrete cylinders (see Figure 10e).

Figure 9b,c compare the mean normal and shear stresses ($\sigma_{n,m}$ and $\tau_{tn,m}$) in the inclined planes for the different layer inclinations, obtained from the applied vertical stress by Equations (7) and (8), respectively. These stresses are mainly relevant for the specimens with $\alpha = 60°$ and 75°, which failed by the concrete layer interface (Figure 10c,d), as they allow to define the strength parameters (the angle of friction and the cohesion) of the assumed Coulomb failure criterion of the interfaces (see Section 4). From the results, it is concluded that a 30-min time gap between the printing of the concrete layers was enough to reduce the interface strength in specimens with 60° and 75° layer inclinations. This result does not depend on other factors that may influence the strength (such as roughness and curing conditions, among others) since failure occurred consistently at the *Cold Joint-30* and not at other joints. However, this study does not allow to draw conclusions on the influence of the time gap, as the experimental campaign did not include samples without no or with longer gap (e.g., 24 h), nor can the results be directly used for other 3DPC processes.

In addition, it should be observed that horizontal friction between the specimen and the top/bottom bearing faces, which is caused by the difference in Poisson ratio, may influence the strength and the failure modes of the specimens.[50–52] It has been experimentally demonstrated that frictional restraint causes an increase of the strength, which instead reduces by increasing the height-to-width ratio, up to a value of 2, beyond which the strength is no longer affected by confinement.[50,51] Moreover, it has been proven that under normal friction between the plates and the specimen, the frictional force is the reason for the inclination of the plane of failure. The triaxially confined regions develop in the specimens at a 45° inclination, with a height equal to half the width of the specimen.[50,51] The confined area comprises most of the specimen for small heights, while its area is relatively smaller for higher height-to-width ratios. As a result, specimens with layer inclinations of 0°, 30°, and 60° are

not influenced by confinement, as the distance between the loading plate and the *Cold Joint-30* is greater than the width of the specimen. However, the failure mode shown in Figure 10e evidences the presence of frictional forces at the ends of the specimen, which cause confinement in the load introduction zones, leading to inclined failures in the concrete. This effect is known and accepted in standard concrete tests to determine the reference strength of concrete. It is expected that the strength in the confined zones will be higher; however, this effect is mitigated for higher h/d ratios ($h/d = 2$ is established for the standard size of cylinder concrete tests). Moreover, according to Figure 10e, it can be seen that the inclined failure plane caused by the confinement at the ends has an angle greater than 75° with respect to the horizontal (critical angle for specimens with slenderness $h/d = 4$). Therefore, an unquantified influence of this confinement to determine a reference strength of 3DPC, including both compressive failures at the matrix or failure at the concrete layer interface (critical for 30 min cold joint at 75°), is acceptable for the authors.

4 | DISCUSSION OF RESULTS AND DERIVATION OF A FAILURE CRITERION FOR 3DPC

In this section, the failure modes are analyzed, and a Mohr's envelope is proposed to characterize the load-bearing capacity of 3DPC elements, including the influence of the layer joints and the cold joint. In addition, some aspects relevant for a design basis of 3DPC are commented.

4.1 | Failure modes

As mentioned in Section 3, two different failure modes of 3DPC were observed in the MSST: (i) matrix failure (Figure 10a,b,e), and (ii) layer interface failure (Figure 10c,d). Both failure modes exhibited a brittle behavior with a sudden drop in the load-bearing capacity after the maximum load was reached. The matrix failure in 3DPC has the same nature as in cast concrete. However, the anisotropy caused by the printing process may result in a premature layer interface failure depending on the orientation of the layer joints, as experimentally observed. The influence of the 3DPC anisotropy is quantified in the following by analyzing the normal σ_n and shear τ_{tn} stresses acting on the concrete layer interfaces at failure observed in the MSST for the different layer inclinations α, noting that layer interface failure depends on these stresses and the strength of the interface. Assuming a Coulomb failure criterion for the joints, the strength of the layer interface is defined by its angle of friction φ_i and cohesion c_i. The differences between these parameters and the angle of (internal) friction φ_c and cohesion c_c of the concrete matrix, respectively, have received little attention in the literature to date, despite the fact that they may differ considerably. In particular, the properties of the concrete layer joints may be affected by the interruption of the printing production (dry or cold joint, time gap of the cold joint), by treatment of the layer surface or by the use of adhesives.

4.2 | Failure criterion of 3DPC

In the following, a failure criterion is defined as a general Mohr's envelope enclosing all stress states that do not cause failure of 3DPC. This envelope is equivalent to yield conditions such as Von Mises and Tresca (incompressible material) or Prager and Drucker (compressible material) established in limit analysis of isotropic materials. Limit analysis of concrete structures[53] commonly relies on a modified Coulomb yield condition (Figure 11), which is a special case of Mohr's envelope complementing Coulomb's failure criterion

$$Y = |\tau| + \sigma \tan(\varphi) - c = 0, \tag{9}$$

by a tension cut-off

$$\sigma < f_{ct}, \tag{10}$$

accounting for the limited tensile strength of concrete. Note that the latter is often neglected in design (i.e., assuming $f_{ct} = 0$). Whereas the dash-dotted lines in Figure 11 apply for general loading, the dashed lines correspond to a compressive failure either in uniaxial or biaxial compression (with the third principal stress equal to zero). Hence, the modified Coulomb yield condition for cases of plane stress is defined by the combination of the dashed and the solid lines. This modified Coulomb yield condition is adopted in the following for the concrete matrix failure.

Due to the anisotropy caused by the layer interfaces, 3DPC may behave differently than cast concrete. However, limit analysis can still be applied to 3DPC by enhancing the yield condition to account for the layer interfaces. To this end, the general Mohr's envelope for 3DPC is defined in the following by complementing the modified Coulomb yield condition of the concrete matrix by a Coulomb failure criterion of the layer joints (Figure 12), using appropriate values for the angle of friction φ_i and the cohesion c_i accounting for the joint type and treatment.

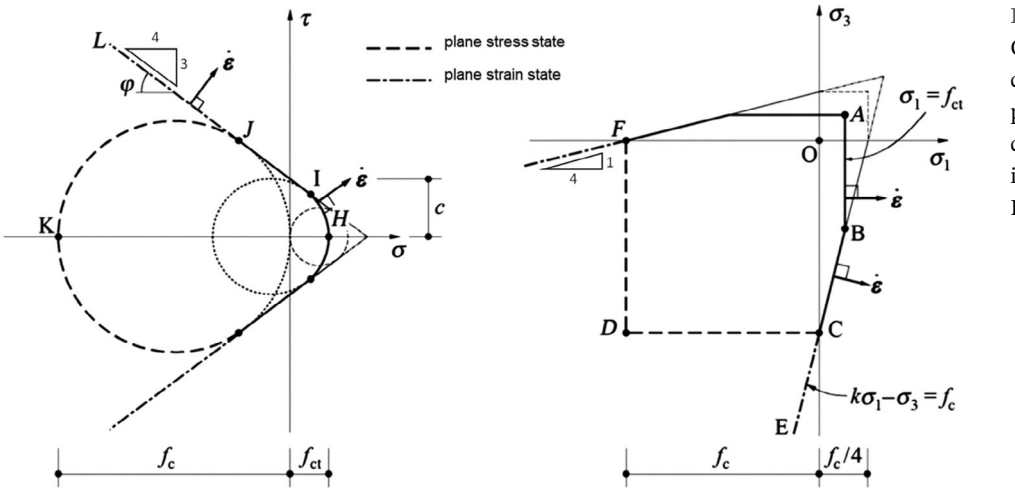

FIGURE 11 Modified Coulomb failure criterion for cast concrete (dashed lines apply to plane stress). Note that for cast concrete typically: $\tan\varphi = 3/4$, that is, $c = f_c/4$. Figure adapted from Ref. 29

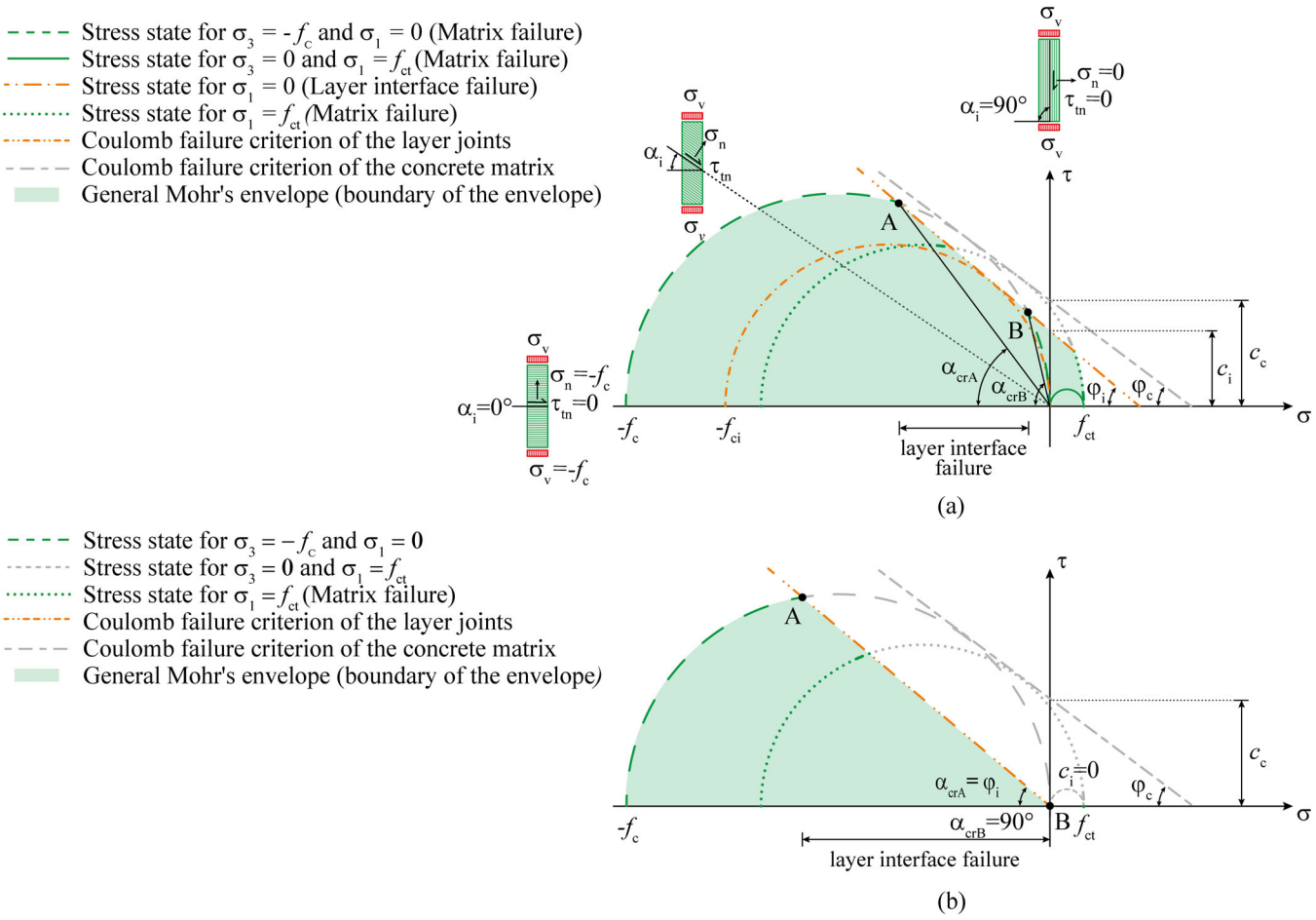

FIGURE 12 Mohr's envelope as failure criterion for 3D printed concrete: (a) cold joint of the concrete layer interface; (b) dry joint of the concrete layer interface.

Figure 12 shows the resulting general Mohr's envelopes (boundary of the shaded areas) of 3DPC in plane stress with cold joints (Figure 12a) and dry joints (Figure 12b), respectively. The latter, which is assumed to lack cohesion ($c_i = 0$) in the layer interface, is a lower bound limit of the failure criterion of cold joints. The modified Coulomb yield condition of the concrete matrix is cut-off by the Coulomb failure criteria of the layer

joints. Both curves intersect in Points A and B, which identify the critical angles α_{crA} and α_{crB} defining the limits between the two failure modes, that is, matrix and layer interface failure. In uniaxial compression (in the MSST), any stress state acting on a plane (on the layer interface) with an inclination α to the plane subjected to the principal compressive stress (to the horizontal plane) lies on the straight line $\tau = -\sigma \tan(\alpha)$, as the pole of Mohr's circle of stresses corresponds to the origin ($\sigma = \tau = 0$). Hence, layer interface failure will govern in a MSST for layer joint inclinations in the critical range $\alpha_{crA} < \alpha < \alpha_{crB}$, while matrix failures are expected for flatter ($\alpha < \alpha_{crA}$) as well as steeper ($\alpha > \alpha_{crB}$) layer interface inclinations, see Figure 12a. In the latter cases, the compressive strength f_c of the concrete matrix will be reached in uniaxial compression (such as in the MSST). On the other hand, for layer inclinations in the critical range $\alpha_{crA} < \alpha < \alpha_{crB}$, a reduced peak compressive stress will be attained, as the layer interface fails at a uniaxial compressive stress smaller than f_c. Based on the strength and failure modes observed in the MSST for the different layer interface inclinations, the general Mohr's envelope of the 3DPC can thus be obtained. Note that a possible non-zero tensile strength of the modified Coulomb yield condition of the matrix is irrelevant as long as no uniaxial or biaxial stress states are considered.

4.3 | Discussion of experimental results

Figure 13 shows the general Mohr's envelopes of 3DPC obtained from the MSSTs performed at 7, 14, and 28 days after the printing, by evaluating the experimental results accounting for the observed failure modes and the layer inclination α. Accordingly, the modified Coulomb yield condition of the concrete matrix is obtained from (i) the average of the peak compressive stress ($\sigma_v = -f_c$) in the specimens exhibiting matrix failure ($\alpha = 0°$, $30°$, and $90°$), (ii) the tensile strength of the concrete matrix, which is estimated as $f_{ct} = f_c/10$ based on the results obtained from the three-point bending tests (see Table 1), and (iii) the angle of (internal) friction, with the corresponding Mohr's circles given by:

$$\left(\sigma + \frac{f_c}{2}\right)^2 + \tau^2 = \frac{f_c}{4}^2$$
$$\left[\sigma - f_{ct} + \frac{c_c - f_{ct}\tan\varphi_c}{\tan((\pi/4) - (\varphi_c/2))}\right]^2 + \tau^2 = \left(\frac{c_c - f_{ct}\tan\varphi_c}{\tan((\pi/4) - (\varphi_c/2))}\right)^2 \quad (11)$$

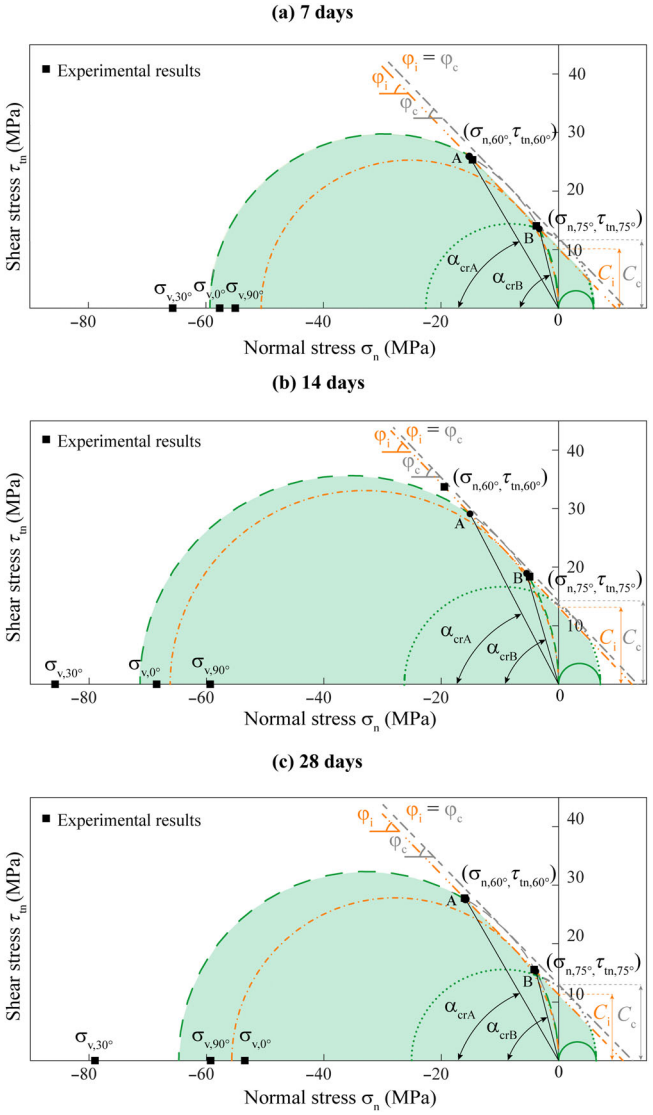

FIGURE 13 Experimental general Mohr's envelopes of 3D printed concrete obtained from the average values of experimental results (see Tables 3 and 4) at different concrete age: (a) 7 days; (b) 14 days; and (c) 28 days.

Note that compressive stresses are negative, but f_c is defined as positive. On the other hand, the Coulomb failure criterion of the layer joints was derived (by linear regression) from the stress states (σ_n and τ_{tn}) in the joint at the peak load of the specimens exhibiting layer interface failures ($\alpha = 60°$ and $75°$), that is,

$$\tau_{tn} = c_i - \sigma_n \cdot \tan(\varphi_i) \quad (12)$$

Be aware that in the evaluation, the cohesion of the concrete matrix c_c is calculated from the experimental results by assuming that the angle of internal friction of

TABLE 4 Experimental parameters of the 3DPC resistance domains at 7, 14, and 28 days shown in Figure 13. Parameters are obtained from the average values of the results.

Days	f_c (MPa)	f_{ci} (MPa)	$f_{ct} = f_c/10$ (MPa)	c_i (MPa)	c_c (MPa)	$\varphi_c = \varphi_i$ (°)	$c_i \cdot \cot(\varphi_i)$ (MPa)	α_{crA} (°)	α_{crB} (°)
7	59.4	50.4	5.9	10.2	12.0	46.1	9.8	59.6	76.4
14	71.2	66.1	7.1	13.2	14.2	46.5	12.5	62.6	73.9
28	63.9	55.5	6.4	11.3	13.0	45.8	11.0	60.1	75.7

the matrix corresponds to that of the layer interfaces, $\varphi_c = \varphi_i$, rather than considering $\tan(\varphi_c) = 0.75$ or $c_c = f_c/4$ as commonly used for cast concrete (Figure 11).

Table 4 summarizes the resulting parameters that define the general Mohr's envelopes of the 3DPC plotted in Figure 13; note that the cohesion c_c of the matrix is smaller than $f_c/4$ (which would result with $\tan(\varphi_c) = 0.75$) and f_{ci} is the (fictitious) uniaxial compressive strength for cohesive layer joints ($c_i > 0$) in arbitrary directions, which is obtained from the Mohr's circle that is tangent to the Coulomb failure criterion of the layer joints (see Figure 12a and see Section 4.4), that is,

$$f_{ci} = \frac{2c_i \cos\varphi_i}{1 - \sin\varphi_i}. \tag{13}$$

The critical angles α_{crA} and α_{crB}, identified by Point *A* and Point *B* (Figure 12), are approximately 60° and 75°, respectively, for the specimens tested at 7, 14, and 28 days (Table 4). The angle of friction φ_i of the concrete layer interface is relatively high, approximately 46°, similar to the value obtained by other researchers for the concrete matrix of 3DPC[26,27] and irrespective of the concrete age, indicating that the layer joints, including the *Cold Joint-30*, did not significantly affect the angle of friction. On the other hand, while the cohesion c_i of the concrete layer interfaces—ranging between 10.2 and 13.3 MPa—was not significantly affected by concrete age, it was roughly 10% smaller than the cohesion of the concrete matrix c_c at the same age (obtained with $\varphi_c = \varphi_i$). Due to this lower cohesion, the layer interfaces cause a slight anisotropy in the strength of 3DPC. Regarding the tensile strength of 3DPC, the obtained strength parameters of the layer interfaces do not correspond to a smaller value than the assumed tensile strength ($f_{ct} = f_c/10 < c_i \cdot \cot(\varphi_i)$), see Table 4. However, direct-tensile tests on the interfaces would be required to validate the interface tensile strength.

As all layer interface failures occurred along the *Cold Joint-30* (30 min time gap), it can be concluded that the regular layer joints had a higher strength than the cold joints; the latter caused the layer interface failures in the specimens with $\alpha = 60°$ and 75° (Figure 10c,d), hence the corresponding reduction of the peak compressive stress by about 10%–20% compared to the specimens with $\alpha = 30°$ (matrix failure).

4.4 | Implications for the design of 3DPC

This study addresses the definition of the 3DPC strength in plane stress by proposing a Mohr's envelope as failure criterion, including a practical test to determine the required strength parameters and an experimental campaign validating the suitability. As the orientation of the layer joints is typically known at the design stage, the strength of the 3DPC can be directly verified using the general Mohr's envelope. On the other hand, if the layer joint orientation has not been defined yet or the (computational) model cannot account for anisotropy, the 3DPC can be modeled conservatively as an isotropic material with a reduced compressive strength f_{ci} (see Table 4), corresponding to that obtained with the strength parameters of the layer joints; note that this corresponds to the assumption of potential layer joints in arbitrary directions.

This study thus contributes to establish a design basis for 3DPC, which, however, needs to cover further aspects, particularly related to dimensioning criteria, manufacturing/printing process, execution, quality control, and maintenance. Specifically, safety factors associated with the mechanical models and the required 3DPC strength need to be defined. As the experimental data collected in the presented study are insufficient to this end, it is essential that other researchers eventually adopt the proposed methodology and increase the volume of available data.

5 | CONCLUSIONS

Nowadays, due to the lack of practical design principles, 3DPC is mainly used as non-load-bearing rather than structural element. In fact, due to the printing process, the 3DPC elements are made of concrete layers, which induce a certain anisotropy in the material, and thus, the standard tests used for cast concrete are not sufficient. This study demonstrates the great potential of the MSST to assess the load-bearing capacity of 3DPC to take into

account the anisotropy of the material. MSST is a simple test and allows determining the main parameters that govern the strength of 3DPC: the compressive strength of the concrete matrix, the cohesion, and the angle of friction of the concrete layer interfaces.

A total of 45 3DPC specimens were tested with different concrete layer inclinations to the horizontal plane ($\alpha = 0°$, 30°, 60°, 75°, and 90°) and at different 3DP concrete ages (7, 14, and 28 days). Each specimen had a cold joint (30 min time gap) to investigate the effects of the interruption of the printing process on the mechanical properties.

In the experimental campaign, two different failure modes were observed depending on the layer inclination: (i) matrix failure (for concrete layer inclination $\alpha = 0°$, 30°, and 90°) and (ii) layer interface failure (for layer inclinations $\alpha = 60°$ and 75°), which occurred at the *Cold Joint-30*, that turned out to be a weak point. The specimens that failed in the layer interface exhibited a reduced strength of about 10%–20% compared to those that exhibited matrix failures. This result is independent of other parameters that may influence the strength (such as roughness and curing conditions, among others) since the failure occurred exactly at the *Cold Joint-30* and not randomly at another joint. On the other hand, the scope of this study also does not allow conclusions to be drawn on the degree of influence of the time gap, as this experimental campaign did not include specimens with concrete layers with no or longer time gaps (e.g., 24 h), nor can the results be directly used for other 3DPC processes.

Based on the experimental observations, a general Mohr's envelope is proposed for defining the strength of 3DPC elements in plane stress, which is a prerequisite for a safe design. The proposed general Mohr's envelope is highly practical, as it is based on the established modified Coulomb yield condition for cast concrete, which is adopted for the printed concrete matrix and enhanced by a Coulomb failure criterion for the layer joints. The latter cuts off the modified Coulomb yield criterion of the concrete matrix, intersecting it in two points that define the critical angles α_{crA} and α_{crB}, which delimit the critical range of layer inclinations $\alpha_{crA} < \alpha < \alpha_{crB}$ (with respect to the plane subjected to the principal compressive stress) for which layer interface failures cause a strength reduction compared to the matrix failure. The peak stresses $\sigma_{n,m}$ and $\tau_{tn,m}$ observed in the specimens with $\alpha = 60°$ and 75° (exhibiting layer interface failure) were used to define the strength parameters (the angle of friction and the cohesion) of the Coulomb failure criterion of the layer joints. The 3DPC elements (all with a 30 min cold joint) exhibited critical angles of $\alpha_{crA} = 60°$ and $\alpha_{crB} = 75°$, and an angle of friction of approximately $\varphi_i = 46°$, similar to that of the concrete matrix documented in recent studies by other authors. However, the cohesion of the concrete layer interfaces, governed by the cold joint, was about 10% lower than that of the concrete matrix. Further research is needed to investigate the effect of a longer time gap and to increase the amount of available data in order to determine safety factors, which are required to design load-bearing 3DPC elements.

As a final remark, the 3DPC material gained its full strength (60 ... 80 MPa) at 14 days after the printing, and about 80% of the maximum strength (55 ... 65 MPa) at 7 days.

AUTHOR CONTRIBUTIONS

Lucia Licciardello: Conceptualization; methodology; investigation; data curation; writing—original draft; writing—review and editing; **Alejandro Giraldo Soto**: Conceptualization; methodology; investigation; data curation; writing—original draft; writing—review and editing. **Walter Kaufmann**: Conceptualization; methodology; writing—review and editing. **Giovanni Metelli**: Conceptualization; writing—review and editing.

ACKNOWLEDGMENTS

The authors would like to acknowledge Prof. Dr. Benjamin Dillenburger, Dr. Ana Anton, and Eleni Skevaki from the Department of Architecture, ETH Zurich, for their support in the printing laboratory. The authors would like to thank Dr. Timothy Wangler of the chair of Physical Chemistry of Building Materials, ETH Zurich, for his contribution to the 3DPC mixture design. The authors would like to recognize Dr. Jaime Mata Falcón of the Chair of Concrete Structure and Bridge Design, ETH Zurich, for the continuous support during the development of the project. A special thanks goes to Prof. Dr. Giovanni Plizzari and Dr. Adriano Reggia from the group of Structural Design at the University of Brescia for enabling the exchange and supervising the research together with Prof. Dr. Walter Kaufmann and Dr. Jaime Mata Falcon. This research is supported by the National Centre for Competence in Research in Digital Fabrication in Architecture, funded by the Swiss National Science Foundation (project number 51NF40-205604). The financial support of the University of Brescia for the doctoral scholarship of the first author is gratefully acknowledged. Open access publishing facilitated by Universita degli Studi di Brescia, as part of the Wiley - CRUI-CARE agreement.

NOTATION

A	width of the 3DPC specimens
$A_{H,eff}$	effective horizontal area
$A_{n,eff}$	effective slanting area
$A_{H,90,eff}$	effective horizontal area for specimen with vertical concrete layer
$A_{r,tot}$	total area of the voids
B	thickness of the 3DPC specimens
b	width of the concrete specimen

c_i	cohesion of the interface
c_c	cohesion of the matrix
d	width of the layer
f_c	compressive strength
f_{ci}	fictitious uniaxial compressive strength for cohesive layer joints
f_{ct}	tensile strength
$f_{ct,fl}$	flexural tensile strength
F_{max}	maximum load
h	depth of the concrete specimen
l	distance between the axis of the support rollers
lp	width of the loading plate
t	thickness of the layer
α	concrete layer inclination to the horizontal plane
$\alpha_{cr,}$	critical angle to define the limits between the two failure modes: matrix and layer interface failure
φ_c	angle of friction of the matrix
φ_i	angle of friction of the interface
σ_v	vertical stresses
σ_n	normal stresses
τ_{tn}	shear stresses

DATA AVAILABILITY STATEMENT

The data that support the findings of this study are available from the corresponding author upon reasonable request.

ORCID

Lucia Licciardello https://orcid.org/0000-0001-5119-7390
Walter Kaufmann https://orcid.org/0000-0002-8415-4896
Giovanni Metelli https://orcid.org/0000-0002-4334-4108

REFERENCES

1. Anton A, Reiter L, Wangler T, Frangez V, Flatt RJ, Dillenburger B. A 3D concrete printing prefabrication platform for bespoke columns. Autom Constr. 2021;122:103467. https://doi.org/10.1016/j.autcon.2020.103467
2. Menna C, Mata-Falcón J, Bos FP, Vantyghem G, Ferrara L, Asprone D, et al. Opportunities and challenges for structural engineering of digitally fabricated concrete. Cem Concr Res. 2020;133:106079. https://doi.org/10.1016/j.cemconres.2020.106079
3. Agustí-Juan I, Habert G. Environmental design guidelines for digital fabrication. J Clean Prod. 2017;142:2780–91. https://doi.org/10.1016/j.jclepro.2016.10.190
4. Flatt RJ, Wangler T. On sustainability and digital fabrication with concrete. Cem Concr Res. 2022;158:106837. https://doi.org/10.1016/j.cemconres.2022.106837
5. Asprone D, Menna C, Bos FP, Salet TAM, Mata-Falcón J, Kaufmann W. Rethinking reinforcement for digital fabrication with concrete. Cem Concr Res. 2018;112:111–21. https://doi.org/10.1016/j.cemconres.2018.05.020
6. Bos FP, Ahmed ZY, Wolfs RJM, Salet TAM. 3D printing concrete with reinforcement. In: Hordijk DA, Luković M, editors. High tech concrete: where technology and engineering meet. Cham: Springer International Publishing; 2018. p. 2484–93. https://doi.org/10.1007/978-3-319-59471-2_283
7. Gebhard L, Bischof P, Anton A, Mata-Falcón J, Dillenburger B, Kaufmann W. Pre-installed reinforcement for 3D concrete printing. In: Buswell R, Blanco A, Cavalaro S, Kinnell P, editors. Third RILEM international conference on concrete and digital fabrication, Digital Concrete 2022. Volume 37. Cham: Springer International Publishing; 2022. p. 430–5. https://doi.org/10.1007/978-3-031-06116-5_64
8. Gebhard L, Esposito L, Menna C, Mata-Falcón J. Interlaboratory study on the influence of 3D concrete printing setups on the bond behaviour of various reinforcements. Cem Concr Compos. 2022;133:104660. https://doi.org/10.1016/j.cemconcomp.2022.104660
9. Gebhard L, Mata-Falcón J, Anton A, Burger J, Lloret-Fritschi E, Reiter L, et al. Aligned interlayer fibre reinforcement and post-tensioning as a reinforcement strategy for digital fabrication. In: Bos FP, Lucas SS, Wolfs RJM, Salet TAM, editors. Second RILEM International Conference on Concrete and Digital Fabrication. Digital Concrete 2020. Volume 28. Cham:Springer; 2020. p. 622–31. https://doi.org/10.1007/978-3-030-49916-7_63
10. Gebhard L, Mata-Falcón J, Anton A, Dillenburger B, Kaufmann W. Experimental investigation of reinforcement strategies for concrete extrusion 3D printed beams. In: Gatuingt F, Torrenti J-M, editors. Proceedings of the 2020 session of the 13th fib International PhD Symposium in Civil Engineering. Lausanne: International Federation for Structural Concrete (*fib*); 2020. https://doi.org/10.3929/ethz-b-000444960
11. Gebhard L, Mata-Falcón J, Anton A, Dillenburger B, Kaufmann W. Structural behaviour of 3D printed concrete beams with various reinforcement strategies. Eng Struct. 2021;240:112380. https://doi.org/10.1016/j.engstruct.2021.112380
12. Gebhard L, Mata-Falcón J, Markić T, Kaufmann W. Aligned interlayer fibre reinforcement for digital fabrication with concrete. In: Serna P, Llano-Torre A, Martí-Vargas JR, Navarro-Gregori J, editors. Fibre reinforced concrete: improvements and innovations, RILEM-fib International Symposium on FRC (BEFIB) in 2020. Volume 30. Cham: Springer International Publishing; 2021. p. 87–98. https://doi.org/10.1007/978-3-030-58482-5_8
13. Mechtcherine V, Buswell R, Kloft H, Bos FP, Hack N, Wolfs R, et al. Integrating reinforcement in digital fabrication with concrete: a review and classification framework. Cem Concr Compos. 2021;119:103964. https://doi.org/10.1016/j.cemconcomp.2021.103964
14. Panda B, Chandra Paul S, Jen TM. Anisotropic mechanical performance of 3D printed fiber reinforced sustainable construction material. Mater Lett. 2017;209:146–9. https://doi.org/10.1016/j.matlet.2017.07.123
15. Bester F, van den Heever M, Kruger J, van Zijl G. Reinforcing digitally fabricated concrete: a systems approach review. Addit Manuf. 2021;37:101737. https://doi.org/10.1016/j.addma.2020.101737
16. Wangler T, Roussel N, Bos FP, Salet TAM, Flatt RJ. Digital concrete: a review. Cem Concr Res. 2019;123:105780. https://doi.org/10.1016/j.cemconres.2019.105780
17. Van Der Putten J, Nerella VN, Mechtcherine V, D'Hondt M, Sonebi M, Weger D, et al. Properties and testing of printed cement-based materials in hardened state. In: Roussel N, Lowke D, editors. digital fabrication with cement-based

materials. Cham: Springer International Publishing; 2022. p. 137–85. https://doi.org/10.1007/978-3-030-90535-4_5
18. Kaliyavaradhan SK, Ambily PS, Prem PR, Ghodke SB. Test methods for 3D printable concrete. Autom Constr. 2022;142:104529. https://doi.org/10.1016/j.autcon.2022.104529
19. Paul SC, Tay YWD, Panda B, Tan MJ. Fresh and hardened properties of 3D printable cementitious materials for building and construction. Arch Civ Mech Eng. 2018;18:311–9. https://doi.org/10.1016/j.acme.2017.02.008
20. Özalp F, Yilmaz HD. Fresh and hardened properties of 3D high-strength printing concrete and its recent applications. Iran J Sci Technol Trans Civ Eng. 2020;44:319–30. https://doi.org/10.1007/s40996-020-00370-4
21. Le TT, Austin SA, Lim S, Buswell RA, Law R, Gibb AGF, et al. Hardened properties of high-performance printing concrete. Cem Concr Res. 2012;42:558–66. https://doi.org/10.1016/j.cemconres.2011.12.003
22. Zareiyan B, Khoshnevis B. Effects of interlocking on interlayer adhesion and strength of structures in 3D printing of concrete. Autom Constr. 2017;83:212–21. https://doi.org/10.1016/j.autcon.2017.08.019
23. Wolfs RJM, Bos FP, Salet TAM. Hardened properties of 3D printed concrete: the influence of process parameters on interlayer adhesion. Cem Concr Res. 2019;119:132–40. https://doi.org/10.1016/j.cemconres.2019.02.017
24. Nerella VN, Hempel S, Mechtcherine V. Effects of layer-interface properties on mechanical performance of concrete elements produced by extrusion-based 3D-printing. Construct Build Mater. 2019;205:586–601. https://doi.org/10.1016/j.conbuildmat.2019.01.235
25. Zareiyan B, Khoshnevis B. Interlayer adhesion and strength of structures in contour crafting – effects of aggregate size, extrusion rate, and layer thickness. Autom Constr. 2017;81:112–21. https://doi.org/10.1016/j.autcon.2017.06.013
26. van den Heever M, du Plessis A, Bester F, Kruger J, van Zijl G. A mechanistic evaluation relating microstructural morphology to a modified Mohr-Griffith compression-shear constitutive model for 3D printed concrete. Construct Build Mater. 2022;325:126743. https://doi.org/10.1016/j.conbuildmat.2022.126743
27. Jayathilakage R, Sanjayan J, Rajeev P. Direct shear test for the assessment of rheological parameters of concrete for 3D printing applications. Mater Struct. 2019;52:12. https://doi.org/10.1617/s11527-019-1322-4
28. EN 12615:1999. Products and systems for the protection and repair of concrete structures: test methods-determination of slant shear strength. Brussels: CEN European Committee for Standardization; 1999.
29. Marti P. Theory of structures: fundamentals, framed structures, plates and shells. 1st ed. Berlin: Ernst & Sohn; 2013.
30. fib. International Federation for Structural Concrete. *fib* Model Code for Concrete Structures 2020. 2023. https://www.fib-international.org/publications/model-codes/model-code-2020.html
31. Pul S, Ghaffari A, Öztekin E, Hüsem M, Demir S. Experimental determination of cohesion and internal friction angle on conventional concretes. ACI Mater J. 2017;114:114. https://doi.org/10.14359/51689676
32. Panda B, Paul SC, Hui LJ, Tay YWD, Tan MJ. Additive manufacturing of geopolymer for sustainable built environment. J Clean Prod. 2017;167:281–8. https://doi.org/10.1016/j.jclepro.2017.08.165
33. Sanjayan JG, Nematollahi B, Xia M, Marchment T. Effect of surface moisture on inter-layer strength of 3D printed concrete. Construct Build Mater. 2018;172:468–75. https://doi.org/10.1016/j.conbuildmat.2018.03.232
34. Reiter L, Anton A, Wangler T, Dillenburger B, Flatt RJ. A 3D printing platform for reinforced printed-sprayed concrete composites. In: Buswell R, Blanco A, Cavalaro S, Kinnell P, editors. Third RILEM International Conference on Concrete and Digital Fabrication, Digital Concrete 2022. Volume 37. Cham: Springer International Publishing; 2022. p. 249–54. https://doi.org/10.1007/978-3-031-06116-5_37
35. Anton A-M. Tectonics of concrete printed architecture: technology, components and assemblies for column-slab construction. Zurich: ETH Zurich; 2022. https://doi.org/10.3929/ETHZ-B-000605076
36. Zanotti C, Borges PHR, Bhutta A, Banthia N. Bond strength between concrete substrate and metakaolin geopolymer repair mortar: effect of curing regime and PVA fiber reinforcement. Cem Concr Compos. 2017;80:307–16. https://doi.org/10.1016/j.cemconcomp.2016.12.014
37. Kreigh JD. Arizona slant shear test: a method to determine epoxy bond strength. ACI J. 1976;73:372–3.
38. Tabor LJ. Evaluation of resin systems for concrete repair. Mag Concr Res. 1978;30:221–5. https://doi.org/10.1680/macr.1978.30.105.221
39. Zanotti C, Randl N. Are concrete-concrete bond tests comparable? Cem Concr Compos. 2019;99:80–8. https://doi.org/10.1016/j.cemconcomp.2019.02.012
40. Zanotti C, Banthia N, Plizzari G. A study of some factors affecting bond in cementitious fiber reinforced repairs. Cem Concr Res. 2014;63:117–26. https://doi.org/10.1016/j.cemconres.2014.05.008
41. Piancastelli EM, Magalhães AG, Silva FJ, Rezende MAP, Santos WJ, Carrasco EVM, et al. Bond strength between old and new concretes with focus on the strengthening of reinforced concrete columns - slant shear test versus double sleeve test. Appl Mech Mater. 2017;864:324–9. https://doi.org/10.4028/www.scientific.net/AMM.864.324
42. Momayez A, Ehsani MR, Ramezanianpour AA, Rajaie H. Comparison of methods for evaluating bond strength between concrete substrate and repair materials. Cem Concr Res. 2005;35:748–57. https://doi.org/10.1016/j.cemconres.2004.05.027
43. Júlio ENBS, Branco FAB, Silva VD, Lourenço JF. Influence of added concrete compressive strength on adhesion to an existing concrete substrate. Build Environ. 2006;41:1934–9. https://doi.org/10.1016/j.buildenv.2005.06.023
44. Saldanha R, Júlio E, Dias-da-Costa D, Santos P. A modified slant shear test designed to enforce adhesive failure. Construct Build Mater. 2013;41:673–80. https://doi.org/10.1016/j.conbuildmat.2012.12.053
45. Hua T, Lin A, Poh WJD, Charlene Y, Wong DHA, Zhang H, et al. 3D-printed concrete shear keys: design and experimental study. Dev. Built Environ. 2023;15:100180. https://doi.org/10.1016/j.dibe.2023.100180
46. Anton A, Lin CW, Skevaki E, Wang M, Wangler T, Flatt R, et al. Tor Alva: a 3D concrete printed tower. London: Fabricate 2024: creating resourceful futures. UCL Press; 2024. p. 252-259. https://doi.org/10.2307/jj.11374766.35
47. EN 1015-11:2020. Method of test for mortar for masonry – part 11: determination of flexural and compressive strength of hardened mortar. 2020. https://www.en-standard.eu/une-en-1015-11-2020-methods-of-test-for-mortar-for-masonry-part-11-determination-of-flexural-and-compressive-strength-of-hardened-mortar/

48. EN 1992-1-1. Eurocode 2: design of concrete structures—part 1–1: general rules, and rules for buildings, bridges and civil engineering structures. Brussels: European Committee for Standardization; 2023.
49. Soto AG, Gebhard L, Anton A, Dillenburger B, Kaufmann W. Structural testing campaign for a 30 m tall 3D printed concrete tower. In: Lowke D, Freund N, Böhler D, Herding F, editors. Fourth RILEM International Conference on Concrete and Digital Fabrication. Digital Concrete 2024. Volume 53. Cham: Springer Nature Switzerland; 2024. p. 493–500. https://doi.org/10.1007/978-3-031-70031-6_57
50. van Mier JGM, Shah SP, Arnaud M, Balayssac JP, Bascoul A, Choi S, et al. Strain-softening of concrete in uniaxial compression: report of the round Robin test carried out by RILEM TC 148-SSC. Mater Struct. 1997;30:195–209. https://doi.org/10.1007/BF02486177
51. Van Vliet MRA, Van Mier JGM. Experimental investigation of concrete fracture under uniaxial compression. Mech Cohesive-Frict Mater. 1996;1:115–27. https://doi.org/10.1002/(sici)1099-1484(199601)1:1<115::aid-cfm6>3.0.co;2-u
52. Talaat A, Emad A, Tarek A, Masbouba M, Essam A, Kohail M. Factors affecting the results of concrete compression testing: a review. Ain Shams Eng J. 2021;12:205–21. https://doi.org/10.1016/j.asej.2020.07.015
53. Nielsen MP, Hoang LC. Limit analysis and concrete plasticity. 3rd ed. Boca Raton: CRC Press; 2011. https://doi.org/10.1201/b10432

AUTHOR BIOGRAPHIES

Lucia Licciardello, Department of Civil, Environmental, Architectural Engineering and Mathematics DICATAM, University of Brescia, Brescia, Italy. Email: l.licciardello@unibs.it.

Alejandro Giraldo Soto, Chair of Concrete Structures and Bridge Design, Institute of Structural Engineering (IBK), ETH Zurich, Zurich, Switzerland. Email: giraldo@ibk.baug.ethz.ch

Walter Kaufmann, Chair of Concrete Structures and Bridge Design, Institute of Structural Engineering (IBK), ETH Zurich, Zurich, Switzerland. Email: kaufmann@ibk.baug.ethz.ch

Giovanni Metelli, Department of Civil, Environmental, Architectural Engineering and Mathematics DICATAM, University of Brescia, Brescia, Italy. Email: giovanni.metelli@unibs.it

How to cite this article: Licciardello L, Soto AG, Kaufmann W, Metelli G. Determining the strength of 3D printed concrete with the modified slant shear test. Structural Concrete. 2025;26(3):2467–86. https://doi.org/10.1002/suco.202400238

APPENDIX A

Tables A1 and A2 reports the results of all the material tests on the 3D printed concrete to derive the compressive strength f_{cm} and the flexural tensile strength $f_{ctm,fl}$. Table A3 reports all the results obtained from the MSST.

TABLE A1 Compressive strength results of 3D printed concrete.

Compressive strength						
Concrete age		**$f_{c\text{-}1}$ (MPa)**	**$f_{c\text{-}2}$ (MPa)**	**$f_{c\text{-}3}$ (MPa)**	**f_{cm} (MPa)**	**σ (MPa)**
7 days	a	47.9[a]	58.4	57.9	57.7	1.34
	b	46.4[a]	55.8	58.8		
14 days	a	66.6	62.9	62.8	63.7	2.20
	b	63.4	65.7	60.5		
28 days	a	64.6	67.1	69.3	66.2	2.31
	b	63.1	65.1	67.9		

[a]Specimens excluded from the average.

TABLE A2 Flexural tensile strength results of 3D printed concrete.

Flexural tensile strength					
Concrete age	**$f_{ct,fl\text{-}1}$ (MPa)**	**$f_{ct,fl\text{-}2}$ (MPa)**	**$f_{ct,fl\text{-}3}$ (MPa)**	**$f_{ctm,fl}$ (MPa)**	**σ (MPa)**
7 days	8.5	10.1	10.1	9.6	0.92
14 days	9.0	11.4	11.7	10.7	1.48
28 days	12.6	12.4	13.2	12.7	0.42

TABLE A3 Modified slant shear test results: maximum force F_{max}, vertical stresses σ_v, normal σ_n, and shear stresses τ_{tn} in the interfaces between concrete layers.

Concrete age	Specimen no.	α (°)	Failure (–)	F_{max} (kN)	σ_v (MPa)	σ_n (MPa)	τ_{tn}(MPa)
7 days	1	0	Concrete	462.74	54.78	54.78	-
	2	0	Concrete	457.23	58.79	58.79	-
	3	0	Concrete	468.62	59.41	59.41	-
14 days	1	0	Concrete	526.55	66.59	66.59	-
	2	0	Concrete	555.15	70.03	70.03	-
	3	0	Concrete	548.02	68.86	68.86	-
28 days	1	0	Concrete	390.11	51.43	51.43	-
	2	0	Concrete	441.00	56.78	56.78	-
	3	0	Concrete	406.81	52.19	52.19	-
7 days	1	30	Concrete	541.40	65.99	49.49	28.57
	2	30	Concrete	528.41	66.24	49.68	28.68
	3	30	Concrete	514.29	64.73	48.55	28.03
14 days	1	30	Concrete	688.97	86.67	65.00	37.53
	2	30	Concrete	673.46	84.90	63.67	36.76
28 days	1	30	Concrete	647.20	81.25	60.94	35.18
	2	30	Concrete	596.73	76.74	57.55	33.23
	3[a]	30	Concrete	512.23	63.95	47.96	27.69

(Continues)

TABLE A3 (Continued)

Concrete age	Specimen no.	α (°)	Failure (–)	F_{max} (kN)	σ_v (MPa)	σ_n (MPa)	τ_{tn}(MPa)
7 days	1	60	Interface CJ30	419.16	52.14	13.04	22.58
	2[b]	60	Concrete	470.61	60.67	15.17	26.27
	3	60	Interface CJ30	520.36	64.89	16.22	28.10
14 days	1	60	Interface CJ30	633.33	77.86	19.46	33.71
	2[b]	60	Concrete	602.48	73.43	18.36	31.80
28 days	1[b]	60	Concrete	420.72	53.73	13.43	23.26
	2	60	Interface CJ30	449.77	56.30	14.08	24.38
	3	60	Interface CJ30	570.52	72.02	18.01	31.19
7 days	1[a]	75	Interface CJ30	336.66	41.39	2.77	10.35
	2	75	Interface CJ30	430.88	55.14	3.69	13.79
	3	75	Interface CJ30	456.88	57.37	3.84	14.34
14 days	1	75	Interface CJ30	587.70	75.46	5.05	18.86
	2[a]	75	Interface CJ30	438.80	51.29	3.44	12.82
	3	75	Interface CJ30	581.55	71.58	4.79	17.89
28 days	1	75	Interface CJ30	409.26	52.37	3.51	13.09
	2	75	Interface CJ30	599.23	75.27	5.04	18.82
	3	75	Interface CJ30	482.18	59.18	3.96	14.80
7 days	1	90	Compression + sliding	627.95	53.64	0.00	0.00
	2	90	Compression + sliding	655.97	56.50	0.00	0.00
	3	90	Compression	637.06	54.87	0.00	0.00
14 days	1	90	Compression	666.68	60.90	0.00	0.00
	2	90	Compression + sliding	589.54	54.28	0.00	0.00
	3	90	Compression	685.15	62.90	0.00	0.00
28 days	1	90	Compression	655.41	57.39	0.00	0.00
	2[a]	90	Compression	565.23	50.93	0.00	0.00
	3	90	Compression	675.39	61.19	0.00	0.00

[a]Results excluded from the average due to excessive imperfection.
[b]Results excluded from the average due to concrete matrix failure.